Volume 13 | Number 25 | 7 July 2017 | Pages 4405–4544

Soft Matter

rsc.li/soft-matter-journal

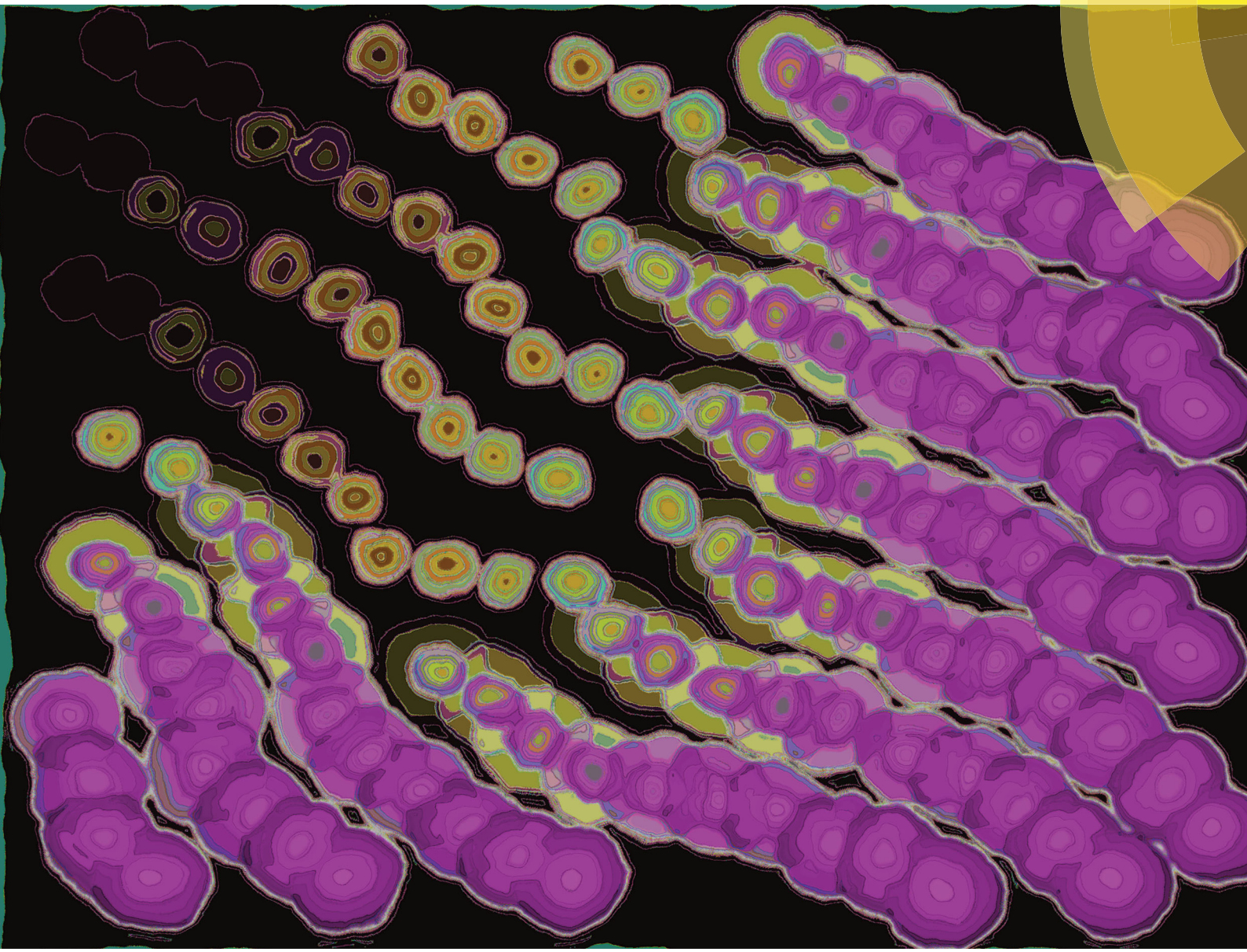

ISSN 1744-6848

ROYAL SOCIETY OF CHEMISTRY

PAPER

Harini Pattabhiraman and Marjolein Dijkstra

On the formation of stripe, sigma, and honeycomb phases in a core–corona system

Soft Matter

PAPER

View Article Online
View Journal | View Issue

Cite this: *Soft Matter*, 2017, **13**, 4418

On the formation of stripe, sigma, and honeycomb phases in a core–corona system

Harini Pattabhiraman and Marjolein Dijkstra*

Using Monte Carlo simulations and free-energy calculations, we investigate the phase behaviour of a two-dimensional core–corona system. We model this system as particles consisting of an impenetrable hard core of diameter σ_{HD} surrounded by a purely repulsive soft corona of diameter $\delta = 1.95\sigma_{HD}$. At low densities, we observe the spontaneous formation of a phase with a stripe texture as well as a honeycomb-like phase driven by both energy and entropy considerations. At high densities, we find that a two-dimensional analogue of the periodic sigma phase, considered as an approximant of dodecagonal quasicrystals, is energetically stabilised with respect to two distinct dodecagonal quasicrystals, namely, a square-triangle tiling and a square-triangle-shield tiling. We also find the formation of stable hexagonal phases at three distinct density ranges, which are energetically driven, *i.e.* by minimising the overlap of coronas. Furthermore, our calculations show that the low-density dodecagonal quasicrystal that was previously reported by Dotera *et al.*, [*Nature*, 2014, **506**, 208] is kinetically formed in the coexistence region between the honeycomb and the medium-density hexagonal phase.

Received 6th February 2017,
Accepted 6th April 2017

DOI: 10.1039/c7sm00254h

rsc.li/soft-matter-journal

I. Introduction

Self-assembly, the process of spontaneous organization of simple components into complex structures, is often controlled by a competition between different interactions in soft matter systems. Anisotropic interactions due to external fields,[1–9] particle shapes,[10–13] particle sizes,[14,15] or surface modifications[16,17] induce the formation of mesophases like stripes,[1,2,5,6,18,19] open structures like honeycomb[3,5,17,20] and Kagome lattices[8,10,16] and even quasicrystals.[14,15,21–27] These open structures and quasicrystals are interesting for their applications as photonic crystals.[28–31] Alternatively, monodisperse colloidal particles interacting with potentials comprising of two length scales can also self-assemble into such phases with non-trivial symmetries. Such systems, which are driven by two competing length scales, are termed as core-softened systems, systems with a core–corona architecture, or simply core–corona systems. Evidences of formation of mesoscale patterns like stripes[32–36] and labyrinths,[33] Archimedean tiling patterns,[22,37] square lattices[38,39] and quasicrystals of various symmetries[39–41] have been reported in core–corona systems.

These core–corona systems can be represented in simulations by a variety of models with different interparticle interactions. In simple terms, three kinds of core–corona interactions can be identified, namely purely attractive or purely repulsive or a combination of the two. Examples of systems with purely attractive interactions include square-well[42] and flat-well[43] pair potentials, that of purely repulsive interactions are square-shoulder[40,44,45] and linear ramp[39] pair potentials, and mixed interactions include Lennard-Jones-Gauss[46] and three-well oscillating[47] pair potentials. Experimentally, these systems consist of spherical particles with a rigid core and a squishy corona, *e.g.*, spherical dendrite micelles consisting of a rigid aromatic core with a deformable shell of alkyl chains,[21] or block copolymer micelles consisting of a micellar core of hydrophobic polymer surrounded by a large shell of hydrophilic polymer blocks.[26]

The interactions observed between these experimental core–corona particles are primarily steric in nature, which results in a strongly repulsive core interaction supplemented with a soft repulsive corona interaction. This form of interaction can be described in terms of three regimes. The first regime occurs at low densities where the coronas do not overlap. The second regime is at high densities, where the coronas entirely overlap and the core repulsion dominates, and finally the third regime is at intermediate densities, where the coronas partially overlap. In this intermediate regime, both the cores and coronas are partially effective and the competition of these core and corona interactions leads to the formation of phases with unusual symmetries. In other words, the minimisation of overlap of the coronas drives the formation of the phases described above.

Although the formation of these mesophases and open structures has been investigated in core–corona systems, the thermodynamic stability of these phases has received less attention. Given that (1) the presence of two-length scales aids

Soft Condensed Matter, Debye Institute for Nanomaterials Science, Department of Physics, Utrecht University, Princetonplein 5, 3584 CC, Utrecht, The Netherlands. E-mail: h.pattabhiraman@uu.nl, m.dijkstra@uu.nl

the formation of quasicrystals in soft-matter systems[37,48–52] and that (2) such two-length scale systems are capable of forming mesophases,[32–36] a question that naturally arises is how the thermodynamic stability of these mesophases and quasicrystals is related to each other in a system that forms both. To the best of our knowledge, we have not come across any such study.

We address these issues in the present work by combining Monte Carlo simulations and free-energy calculations. We evaluate the thermodynamic stability of a mesophase, open structures and quasicrystals formed in a core–corona system. We model this system by using two-dimensional disks with diameter σ_{HD} interacting with a hard core and a purely repulsive square-shoulder potential at a fixed shoulder width of $1.95\sigma_{HD}$. We find the formation of a stripe, honeycomb and sigma phases along with hexagonal and fluid phases in this system. This paper is organised as follows. In Section II, we introduce the model and describe the simulation methods that we employ to study the phase behaviour of this system. We present the results regarding the formation and stability of a striped mesophase, quasi-periodic and periodic phases in Section III and we end with an overview of the phase behaviour in our conclusions in Section IV.

II. Methods

A. Model and simulations

The core–corona model used in this study consists of a two-dimensional system of spherical particles interacting with a hard-core square shoulder (HCSS) pair potential $V_{HCSS}(r)$. This radially symmetric pair potential consists of a hard core of diameter σ_{HD} and a purely repulsive square shoulder of diameter δ and reads

$$V_{HCSS}(r) = \begin{cases} \infty, & r \le \sigma_{HD} \\ \varepsilon, & \sigma_{HD} < r \le \delta \\ 0, & r > \delta \end{cases} \quad (1)$$

where r is the interparticle centre-of-mass distance, and $\varepsilon > 0$ is the height of the square shoulder. Fig. 1 shows a schematic representation of this pair potential, where the hard core and square shoulder are represented by the dark and light red circles. The HCSS potential introduces two characteristic length scales in the system; one at the diameter of the hard core σ_{HD} and the other one at the soft shoulder δ. The latter is the only tunable parameter for studying the system. It has been previously shown by Dotera *et al.*[40] and Schoberth *et al.*[41] that quasicrystals of various symmetries form at specific values of δ. In this work, we use a value of $\delta = 1.95\sigma_{HD}$. This chosen shoulder width is close to (1) the shoulder width of $\delta = 2.0\sigma_{HD}$[53,54] and $\delta = 2.5\sigma_{HD}$[32,34,36] where stripe phases have previously been reported in certain computational studies as well as (2) the irrational ratio of $2\cos 15^\circ \approx \sqrt{2+\sqrt{3}} \approx 1.932$ where quasicrystals of dodecagonal symmetry at a high density have been reported to form in various theoretical and/or computational studies.[40,46,48,50,55] Thus, this shoulder width is an ideal starting point to locate both the stripe phase and the dodecagonal quasicrystal. Furthermore, a dodecagonal quasicrystal at a lower density has also been reported by Dotera *et al.* at this shoulder width of $\delta = 1.95\sigma_{HD}$.[40]

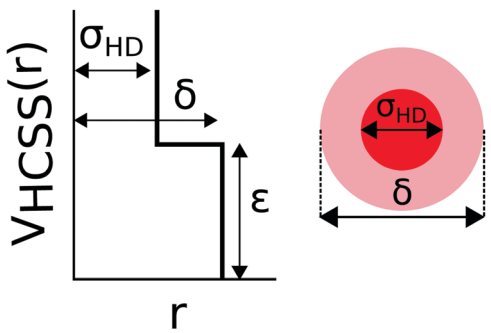

Fig. 1 Schematic representation of the hard-core square shoulder (HCSS) potential, $V_{HCSS}(r)$, as a function of the interparticle distance r. The dark and light circles respectively represent the hard core and the soft corona.

To address the phase behaviour of this system and the relative stability of various phases, we perform Monte Carlo (MC) simulations in a rectangular box of area A with periodic boundary conditions in the canonical (NVT) and isothermal–isobaric (NPT) ensembles. We choose σ_{HD} and ε, respectively, as the units of length and energy, and define a reduced temperature $T^* = k_BT/\varepsilon$, reduced pressure $P^* = \beta P\sigma_{HD}^2$, and a reduced density $\rho^* = N\sigma_{HD}^2/A$, where $\beta = 1/k_BT$ is the inverse temperature with k_B the Boltzmann constant. In the simulations, we use a system size between 209 to 256 particles depending on the initial crystal structure, while a system size of 1600 particles was used in case of an isotropic fluid phase as initial configuration.

B. Phase diagram construction

We determine the phase diagram of the system in a three-step process. In the first step, we measure the isotherms of the equation of state (EOS) of the phases of interest at a fixed temperature T^*. These isothermal EOS, *i.e.* the bulk pressure P^* as a function of the equilibrium density ρ^*, are obtained by performing compression and expansion runs by either increasing or decreasing the pressure P^* in a step-wise manner in the NPT ensemble. We start the compression runs from a disordered isotropic fluid phase, while the expansion runs are started using a crystal or a quasicrystal phase. In the second step, we determine the dimensionless Helmholtz free energy per particle $f = \beta F/N$ as a function of density at a fixed temperature T^* for each of the observed phases. This is done by thermodynamic integration of the EOS to a reference density. The free energy at this reference density is calculated by constructing a reversible thermodynamic path to a reference system for which the free energy can be calculated analytically. We employ the hard-disk fluid phase at the same density as a reference state for the fluid phase,[56,57] and the non-interacting Einstein crystal[56,58,59] as a reference for the periodic crystals. For all other phases in the system, namely the quasicrystal, its approximants, and the stripe phase, we use a non-interacting system of particles pinned by an attractive linear well[60,61] to their reference positions as a reference system. In the final step, we employ a common tangent construction to the free-energy curves, *i.e.*, the Helmholtz free energy per unit area $\beta F/A$

as a function of reduced density ρ^*, to determine the thermodynamically stable phases and the corresponding phase boundaries.

Additionally, we also monitor the nature of phase transitions in the *NVT* ensemble by calculating the specific heat C_v at constant volume defined by

$$C_v = \frac{\langle U^2 \rangle - \langle U \rangle^2}{k_B T^2} \quad (2)$$

where U is the potential energy of the system.

C. Structural analysis

We calculate various order parameters to study the local structure and to differentiate between the phases. This includes the radial distribution function (RDF) of the system $g(r)$, the static structure factor $S(k)$, and the average m-fold bond orientational order parameter (BOO) of the system χ_m. In addition, we calculate the polygonal tiling corresponding to each structure. Furthermore, we also employ a local particle environment analysis to characterise the quasicrystals and an anisotropic scaling method to identify the stripe phases. Each of these analysis methods is explained below.

The RDF of a system at density ρ^* gives the probability of finding a pair of atoms at a distance $r = |\mathbf{r} - \mathbf{r}'|$, and reads

$$g(r) = \frac{1}{\rho^{*2}} \left\langle \sum_{i=1}^{N} \sum_{j \neq i}^{N} \delta(\mathbf{r} - \mathbf{r}_i) \delta(\mathbf{r}' - \mathbf{r}_j) \right\rangle, \quad (3)$$

where $\mathbf{r}_i$ and $\mathbf{r}_j$ are the positions of particles i and j, respectively. The static structure factor $S(k)$ is obtained by a Fourier transformation of the RDF and is written as

$$S(k) = \frac{1}{N} \langle \rho_{\mathbf{k}} \rho_{-\mathbf{k}} \rangle = \frac{1}{N} \left\langle \sum_{i=1}^{N} \sum_{j \neq i}^{N} \exp -i\mathbf{k} \cdot (\mathbf{r}_i - \mathbf{r}_j) \right\rangle, \quad (4)$$

where $\rho_{\mathbf{k}}$ is the Fourier transform of the microscopic density $\rho(r)$. The structure factor is represented in two-dimensional space as a diffraction pattern. The BOO is defined as[62]

$$\chi_m = \left\langle \left| \frac{1}{N_B(i)} \sum_{j=1}^{N_B(i)} \exp(im\theta_{\mathbf{r}_{ij}}) \right|^2 \right\rangle, \quad (5)$$

where m is the integer associated with the symmetry of interest, $\mathbf{r}_{ij} = \mathbf{r}_i - \mathbf{r}_j$ is the vector connecting the center-of-mass of two neighbours, $\theta_{\mathbf{r}_{ij}}$ is the angle between $\mathbf{r}_{ij}$ and an arbitrary axis, and $N_B(i)$ is the number of neighbours of particle i. We identify the neighbours of particle i as particles that are at a center-of-mass distance smaller than the square shoulder diameter δ from particle i. Clusters are identified as collections of neighbouring particles and the corresponding polygonal tiling is constructed by drawing bonds between the neighbouring particles. Additionally, we also calculate the bond orientational correlation function as

$$g_m(r) = \langle \chi^j{}_m(\mathbf{r}' + \mathbf{r}) \cdot \chi^{k*}_m(\mathbf{r}') \rangle. \quad (6)$$

In the case of the dodecagonal quasicrystal phase and its approximants, we also calculate the local particle environment (LPE) to differentiate between the σ and H environments[63] as shown in Fig. 2. The H and σ LPEs respectively correspond to Archimedean tilings (3^34^2) and (3^2434).[63]

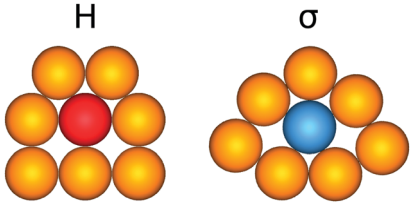

Fig. 2 Schematic overview of the H and σ local particle environments (LPE).

We utilise an anisotropic scaling index method to distinguish between the fluid and stripe phases.[64,65] Here, a weighted scaling index α of the system is calculated as

$$\alpha = \frac{\left\langle \sum_{i=1}^{N} \sum_{j \neq i}^{N} \delta(\mathbf{r} - \mathbf{r}_i) \delta(\mathbf{r}' - \mathbf{r}_j) q (r_c / r_{ij})^q e^{-(r_c/r_{ij})^q} \right\rangle}{\left\langle \sum_{i=1}^{N} \sum_{j \neq i}^{N} \delta(\mathbf{r} - \mathbf{r}_i) \delta(\mathbf{r}' - \mathbf{r}_j) e^{-(r_c/r_{ij})^q} \right\rangle} \quad (7)$$

where $r_{ij} = |\mathbf{r}_i - \mathbf{r}_j|$ is the distance between particles i and j at positions $\mathbf{r}_i$ and $\mathbf{r}_j$, r_c is a cut-off distance, and q is a control parameter. In this study, the cut-off distance r_c is taken to be $2.5\sigma_{HD}$ and the control parameter q is set to 2. The index α is a local non-linear measure used to characterise the symmetry of the structure along a certain direction. The change in symmetry of the system due to the formation of stripes can then be quantified by the probability distribution functions of α in the directions parallel and perpendicular to the stripes. Hence, a scalar order parameter to quantify the transition between fluid and stripe phases is defined as the difference between the average parallel and perpendicular scaling indices,[64,65]

$$\Delta\alpha = \int \alpha P_\perp(\alpha) d\alpha - \int \alpha P_\parallel(\alpha) d\alpha. \quad (8)$$

III. Results and discussion

In this section, we first present the phase diagram of the HCSS system with a shoulder width $\delta = 1.95\sigma_{HD}$ and then separately examine the formation and stability of the different phases.

The phase behaviour at the chosen shoulder width is particularly interesting due to the comparative sizes of the shell of the soft corona ($0.95\sigma_{HD}$) and the diameter σ_{HD} of the hard core. Consequently, the interplay between energy and entropy determines the peculiar phases formed at low and intermediate densities. We show the calculated phase diagram in the (reduced) temperature T^*–density ρ^* representation in Fig. 3a and b, along with typical configurations of the various phases in the core-shoulder representation. We also take a closer look at the low-temperature regime of this phase diagram in the (reduced) pressure P^*–temperature T^* representation in Fig. 3c. From these figures, it is clear that the system shows a rich phase behaviour with a fluid (FL) phase, a stripe (STR), a honeycomb (HC), and a sigma (SIG) phase, and hexagonal phases at three distinct density ranges, namely a low-density (LDH), a medium-density (MDH), and a high-density (HDH) hexagonal

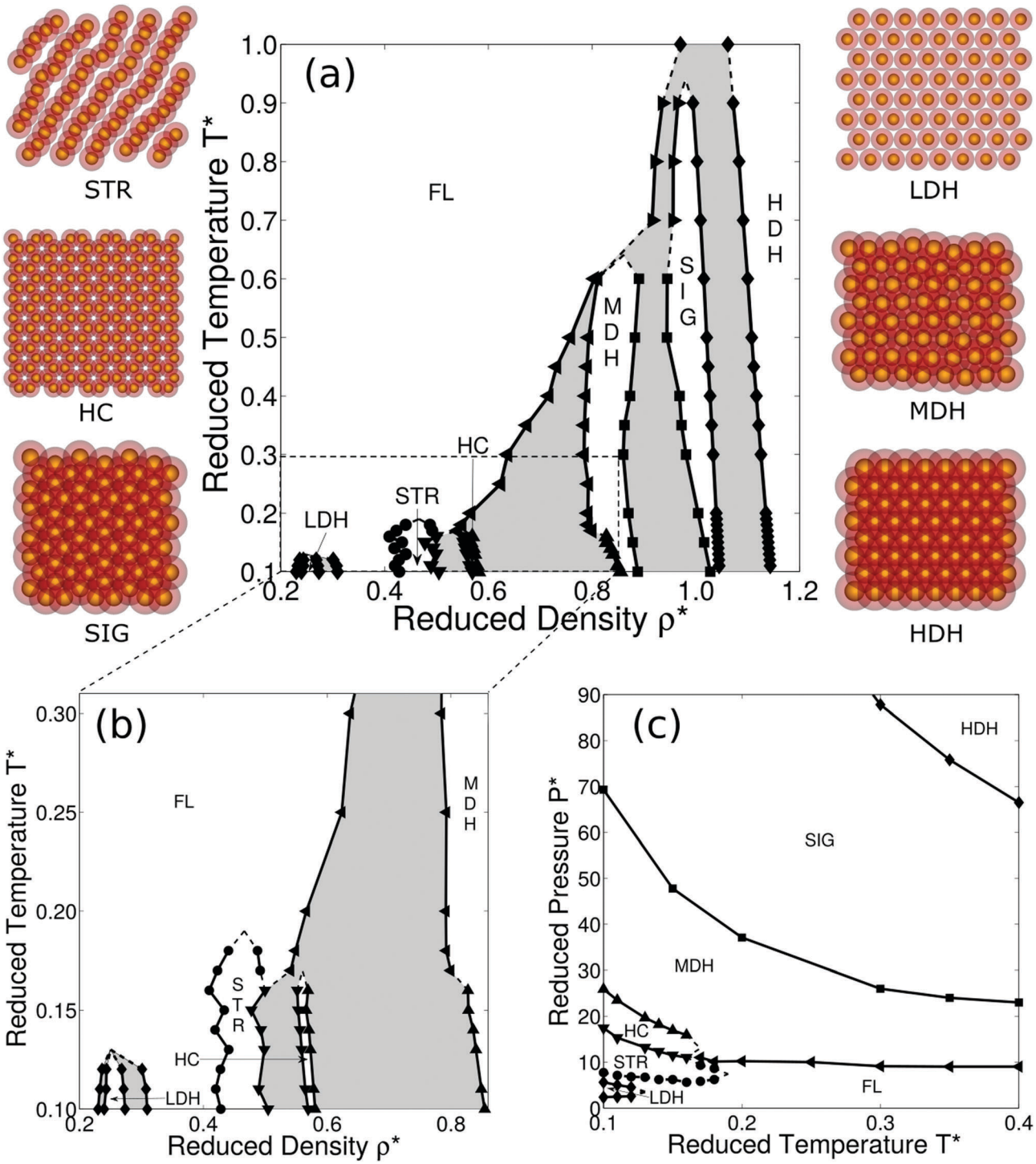

Fig. 3 (a) Phase diagram of the HCSS system with a shoulder width $\delta = 1.95\sigma_{HD}$ in the (reduced) temperature T^*–density ρ^* plane. A zoomed in version of the phase diagram in the low-temperature regime is given in (b) in the (reduced) temperature T^*–density ρ^* plane and (c) in the (reduced) pressure P^*–temperature T^* plane. The reduced quantities are defined as $T^* = k_BT/\varepsilon$, $\rho^* = N\sigma_{HD}{}^2/A$ and $P^* = \beta P\sigma_{HD}{}^2$. The stable phases include fluid (FL), stripe (STR), honeycomb (HC), low-density hexagonal (LDH), medium-density hexagonal (MDH) and high-density hexagonal (HDH) and sigma (SIG) phases. The grey areas denote the coexistence regions between two phases. Typical configurations of the phases obtained from Monte Carlo simulations are shown on either side of (a). The hard cores are coloured in yellow and the soft coronas in red.

phase. The SIG phase is a periodic approximant of a dodecagonal quasicrystal and is named after its three-dimensional analogue of the Frank–Kasper phase.[63,66]

At low temperatures and densities, we recognise a re-entrant behaviour of the FL phase encompassing the LDH phase. At moderate densities, we find the STR and HC phases at low

temperatures $T^* < 0.20$ and a broad two-phase coexistence region between the HC and MDH phases. On the other hand, at $T^* > 0.20$, the STR and HC phases are unstable and we find a broad coexistence between the FL and MDH phases. With increasing densities, three crystal phases are observed in this system, namely the MDH, SIG and HDH phases. At much higher temperatures, $T^* > 0.6$ and $T^* > 0.9$, the MDH and STR phases respectively are unstable and the system displays hard-disk like behaviour described by the FL at low densities and HDH at high densities with a two-phase coexistence region in between. We individually examine the formation and stability of each of these phases in the following sections.

A. Formation of the hexagonal phases

We begin with the formation of the three different hexagonal phases observed in this system. With the inherent presence of two length scales in the system, the presence of two hexagonal phases in the system is self-evident. The inter-particle distance in these two hexagonal phases is expected to correspond to the diameter of the core σ_{HD} and the diameter of the corona δ. However, at this shoulder width $\delta = 1.95\sigma_{HD}$, we observe three distinct hexagonal phases instead of the expected two! In order to investigate the formation of these three phases, we calculate their radial distribution function (RDF) $g(r)$ and plot them in Fig. 4.

Consistent with the above expectation of the two hexagonal phases, we indeed notice that the first peak of the RDF of the HDH and LDH phases lies respectively at a distance r that equals σ_{HD} and δ. This confirms their inter-particle distances at the diameters of the core and corona, respectively. The puzzling question is the formation of the MDH phase. From the RDF, we note that the first peak corresponds to an inter-particle distance that lies in between the core and corona diameters, and the second peak corresponds to a distance that equals the corona diameter δ. This means that the corona limits the position of the second nearest neighbours and thus, results in the formation of the MDH. This difference in the inter-particle distance between the three structures can also be seen in terms of the overlaps of the coronas as observed in the configurations given in Fig. 3. For the LDH phase, the corona of a particle is in contact with the coronas of its neighbouring particles. On the other hand, for the HDH phase the cores are in contact, *i.e.* the corona of the particle entirely overlaps with the core of its neighbouring particles. For the MDH structure, the corona of a particle just touches the corona of its second nearest neighbours.

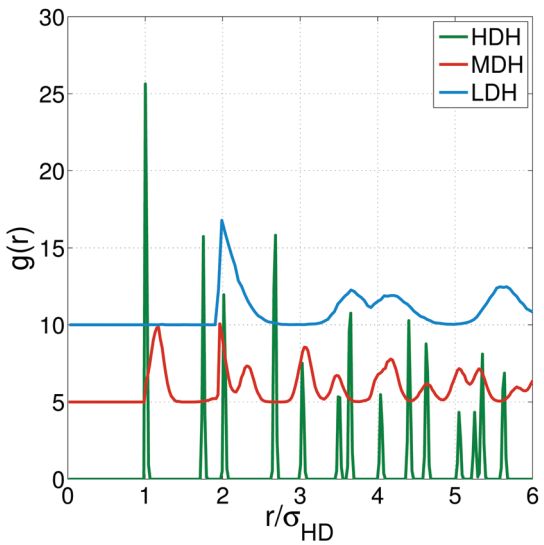

Fig. 4 Radial distribution functions $g(r)$ calculated for the low-density (LDH), medium-density (MDH) and high-density (HDH) hexagonal phases. For clarity, we shifted the $g(r)$ in the vertical direction by $\Delta y = 5$.

B. Formation and stability of the sigma-phase and dodecagonal quasicrystals

As previously mentioned, the chosen shoulder width $\delta = 1.95\sigma_{HD}$ is close to the value of $2\cos 15° \approx \sqrt{2+\sqrt{3}} \approx 1.932$ at which random-tiling dodecagonal (12-fold symmetric) quasicrystals have been reported either theoretically and/or computationally in various systems.[40,46,48,50,55] Hence, we also expect the formation of a similar quasicrystal phase in the system under investigation.

In order to address this possibility, we obtain the equation of state (EOS) by expanding the system starting from a high-density hexagonal (HDH), a defect-free random tiling dodecagonal quasicrystal (HQC), or either of the two dodecagonal approximant crystals considered in this study, namely the sigma (SIG) phase and a square-triangle tiling of dodecagons (HAC). The high-density quasicrystal (HQC) structure is adapted from a non-Stampfli square-triangle approximant.[67] The HQC is similar in structure to the dodecagonal quasicrystal previously reported by Dotera *et al.* in a HCSS system at $\delta = 1.4\sigma_{HD}$,[40] but without the presence of any tiling defects as described in our previous work.[38] The SIG structure is a periodic representation of the σ particle environment with a unit cell consisting of 32 particles. The high-density approximant crystal (HAC) is an adaptation of a repeated vertex substitution of the $(3^2{\cdot}4.3.4)$ Archimedean tiling consisting of squares and triangles.[68] It has a unit cell of 56 particles and contains both σ and H particle environments. Fig. 5 shows a comparison between the quasicrystal HQC and the two approximants, *i.e.* the SIG and HAC phase, where a representative configuration is given on the left and its accompanying tiling on the right. The particles in the configurations are coloured according to the LPEs described in Section II C. From this colouring, we can see that the HQC has a higher H/σ LPE ratio than the HAC. In the EOS calculations, we use a system size of 209 particles for the HQC, 288 particles for SIG and 224 particles for the HAC, and 256 particles for the HDH phase.

In Fig. 6a, we plot the EOS articulating the various expansion runs, *i.e.* decreasing pressure P^*, starting from the HDH, SIG and HQC phases. We exclude the EOS of the HAC phase for clarity as it is qualitatively similar to that of the HQC phase. From the EOS shown in Fig. 6a, we observe a single phase transition around $P^* = 30$ during the expansion of the SIG phase, *i.e.* upon decreasing pressure. However, in the case of the expansion of the HDH and HQC phases, we find an additional transition at pressures higher than $P^* = 30$ resulting into a structure with a density lower than that of the SIG phase. To investigate the nature of the resulting structure, we calculate

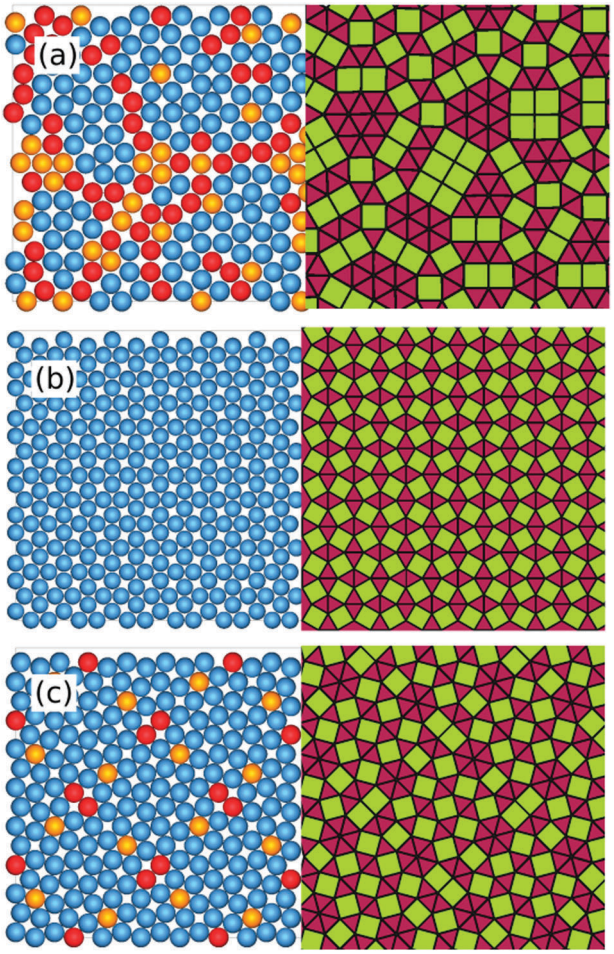

Fig. 5 Structural difference between the dodecagonal quasicrystal and its approximants (a) defect-free random-tiling quasicrystal (HQC) (b) sigma (SIG) (c) square-triangle tiling of dodecagons (HAC). (left) A typical configuration is shown on the left with the particles coloured according to their local particle environment (LPE) described in Section II C: H in red and σ in blue and particles not belonging to either in orange. (right) The tiling obtained by drawing bonds between the neighbouring particles.

the BOO parameter and determine the different LPEs in the system as explained in Section II C.

Let us first consider the behaviour of the BOO parameter of this system. We calculate the χ_6 and χ_{12} order parameters, which quantify the hexagonal and dodecagonal order in the system. In Fig. 6b–d, we plot χ_6 and χ_{12} during the expansion of the HDH, SIG and HQC structures, respectively. During the expansion of the HDH phase in Fig. 6b, we find that χ_6 has a higher value than χ_{12} at higher ($48 \leq P^* \leq 70$) and lower ($15 \leq P^* \leq 33$) pressures, while χ_{12} is only slightly higher than χ_6 at intermediate ($33 \leq P^* \leq 48$) pressures. This implies the presence of three distinct regions namely of hexagonal, dodecagonal, and hexagonal order. The decrease in χ_{12} during the expansion of the SIG phase in Fig. 6c at $P^* = 30$ denotes a transition from dodecagonal to hexagonal order. The behaviour of χ_{12} during the expansion of the HQC phase in Fig. 6d is peculiar. Upon decreasing the pressure, we find a drop in the value of χ_{12} at $P^* = 44$ coinciding with the discontinuity in the EOS; while that of χ_6 remains unchanged. This indicates the presence of two different structures of dodecagonal symmetry in between the two with a hexagonal order.

To differentiate between the two structures with dodecagonal symmetry, we calculate the fraction of H and σ particle environments. The fraction of H (f_H) and σ (f_σ) particle environments as a function of pressure obtained by expanding the HDH, SIG and HQC structures are plotted in Fig. 6e–g. In Fig. 6e we notice a sizeable fraction of σ environments at intermediate pressures which conforms with the previously observed increase in χ_{12} at these pressures ($33 \leq P^* \leq 48$). The lower fraction of H environments in comparison to σ is also interesting to note. In Fig. 6f, we observe that the fraction of σ environments drops from one to zero at $P^* = 32$ during the expansion of the SIG phase and we do not observe any significant fraction of H environments. In Fig. 6g, the change in both the fraction of H and σ environments coincides with the decrease in χ_{12} at $P^* = 44$ during the expansion of HQC phase in Fig. 6d. However, we note that the fraction of H environments drops close to zero whereas the fraction of σ environments remains close to the previous non-zero value. Thus, considering the presence of a sizeable fraction of H-phase and a lower density than that of the SIG phase as shown by the EOS, we suggest that the HQC transforms to a σ-rich phase and not the SIG phase.

We further analyse the σ-rich phase by comparing the configurations obtained just before ($P^* = 44$) and after ($P^* = 43$) the transition during the expansion of HQC phase in Fig. 7. The particle configuration is shown on the left and its accompanying tiling obtained by drawing bonds between the neighbouring particles is shown on the right. The inset shows the calculated diffraction pattern. It can be noted from the inset that both structures posses dodecagonal symmetry. Furthermore, we also note the difference between the tilings of the two structures: the HQC phase shown in Fig. 7a consists of a square-triangle tiling while the σ-rich phase shown in Fig. 7b consists of a square-triangle-shield tiling. Though the square-triangle tiling is the most common description of a dodecagonal quasicrystal tiling, tilings involving shields and/or rhombi are not uncommon.[20,69–72] Therefore, we term this σ-rich phase as a quasicrystal with shields (QCS). It is surmised that upon decreasing the pressure, the simultaneous decrease in density and preservation of the dodecagonal symmetry is made possible by the formation of shields which have a larger area than the combination of squares and triangles. In summary, we find four structures with dodecagonal symmetry, *i.e.* the two approximant crystals, which are the sigma (SIG) phase and the square-triangle tiling of dodecagons (HAC), and the high-density random-tiling dodecagonal quasicrystal (HQC) with a square-triangle tiling and the quasicrystal with shields (QCS).

Subsequently, we deduce the stable phases by calculating the free energies and employing common tangent constructions as explained in Section II B. In Fig. 8a, we show the common tangent construction between the SIG and the MDH phase at temperature $T^* = 0.20$ and in Fig. 8b, between the SIG and HDH phases at $T^* = 0.70$. In both these figures, we plot the Helmholtz free energy per unit area $\beta F/A$ as a function of reduced density ρ^*. We then subtract a linear fit $\rho\mu_c - P_c$ from the free energy,

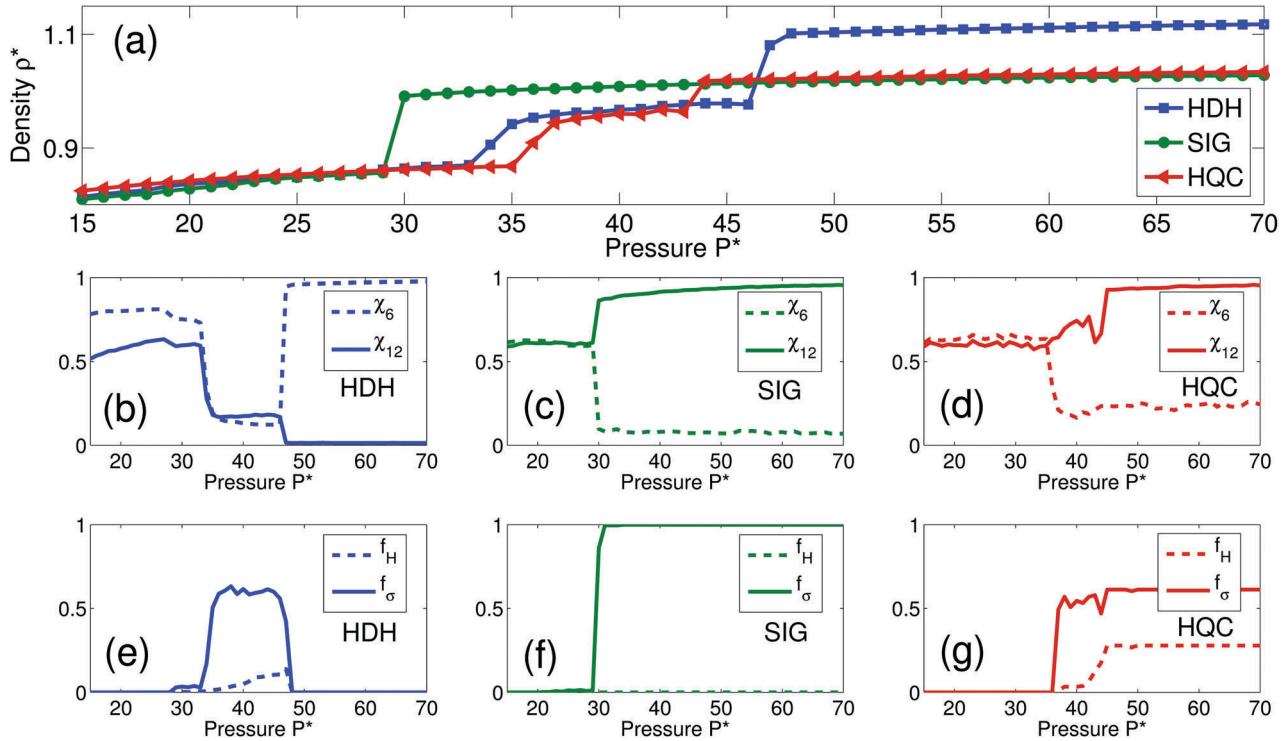

Fig. 6 Formation of a 12-fold symmetric phase at $T^* = 0.20$ as obtained by expanding the high-density hexagonal (HDH,) sigma (SIG) and random-tiling dodecagonal quasicrystal (HQC) phase in a HCSS system with shoulder width $\delta = 1.95\sigma$. (top) Density $\rho^* = N\sigma^2/A$ (equation of state), (middle) bond orientational order (BOO) parameter χ_6 and χ_{12}, and (bottom) fraction of H and σ environments, f_H and f_σ, as a function of the reduced pressure $P^* = \beta P\sigma^2$.

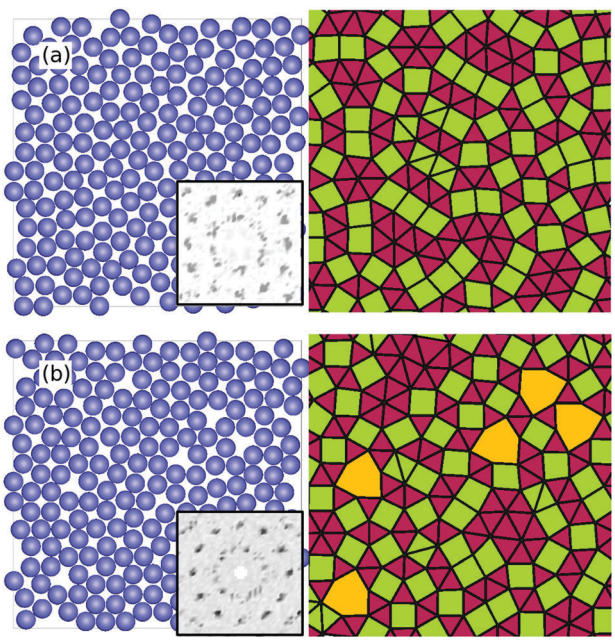

Fig. 7 Structural difference between the two random-tiling dodecagonal quasicrystals with (a) square-triangle tiling (HQC) at $P^* = 44$ (b) square-triangle-shield tiling (QCS) at $P^* = 43$ for a HCSS system with shoulder width $\delta = 1.95\sigma_{HD}$ at temperature $T^* = k_BT/\varepsilon = 0.20$. A typical configuration is shown on the left with the calculated diffraction pattern in the inset. The tiling obtained by drawing bonds between the neighbouring particles is given on the right.

where μ_c is the bulk chemical potential of the coexisting phases at pressure P_c. This ensures that the 'resulting' free energy of the two-phases between which the common-tangent is drawn is zero at the coexistence densities. In other words, the phases with a positive free energy in this plot are meta-stable with respect to the concerned two-phase coexistence. Based on this, it is conspicuous from both Fig. 8a and b that the SIG is more stable than all other phases exhibiting dodecagonal symmetry,

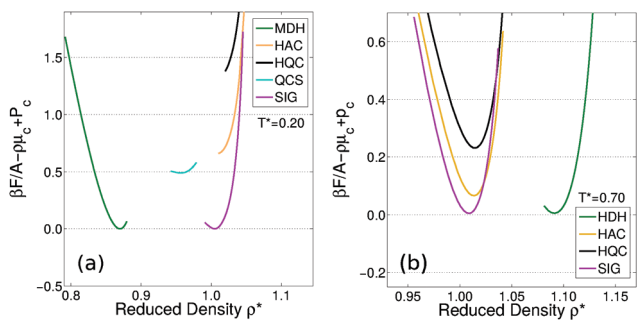

Fig. 8 Common tangent construction to determine the stable phases in the HCSS system with shoulder width $\delta = 1.95\sigma_{HD}$. The common tangent is constructed between (a) MDH and SIG phases at $T^* = 0.20$ (b) the SIG and HDH at $T^* = 0.70$. The involved phases are the medium-(MDH) and high-density hexagonal (HDH) phases and the sigma phase (SIG). Other phases exhibiting 12-fold symmetry that are plotted are the approximant crystal (HAC) and the random-tiling quasicrystal with a square-triangle (HQC) and a square-triangle-shield (QCS) tiling. The reduced temperature is expressed as $T^* = k_BT/\varepsilon$.

namely the HAC, HQC and QCS phases. Also, as (not) shown in Fig. 8b, we do not find the formation of the QCS phase at higher temperatures.

It is intriguing to note that the free energy of the phases under the present conditions (SIG < HAC < HQC) contrasts to that reported at $\delta = 1.40\sigma_{HD}$,[38] where the free energy increased in the order of HQC < HAC < SIG. To further investigate this, we first eliminate the effect of finite system size on the free energy. To do so, we evaluate the variation in potential energy and Helmholtz free energy as a function of system size for these three phases. Fig. 9 shows the calculations performed at $\rho^* = 1.03$ and $T^* = 0.11$ at different system sizes. In Fig. 9a–c, we individually show the variation in free energy per particle as a function of inverse system size for the SIG, HAC and HQC phases. Fig. 9d is a combination of these three plots. We can extrapolate the free energy to the thermodynamic limit $1/N \to 0$ by calculating the intercept of these curves. We obtain the following values of bulk free energies, $\beta F/N = 43.22$ (SIG), 44.73 (HAC) and 45.82 (HQC). This shows that the SIG phase has the lowest free energy among the three phases. We also find that the difference between the free energies of the three phases is much larger than the variation in the free energy of individual phases as a function of system size. The surprising part is the difference in potential energy per particle in these phases as shown in Fig. 9e. As previously studied, the potential energy per particle for these phases at $\delta = 1.4\sigma$ is similar.[38] However, here, we find the potential energy increases in the order SIG < HAC < HQC. This is, obviously, caused by the difference in the shoulder width of these two systems. For the system at $\delta = 1.4\sigma_{HD}$, only the nearest neighbours contribute to the potential energy of the particles. However, in the present system with $\delta = 1.95\sigma_{HD}$, the second nearest neighbours of particles at a distance $1.4\sigma_{HD} < r < 1.95\sigma_{HD}$ also contribute to the potential energy. In other words, not only does the composition of a structure in terms of its LPE matters, but also the arrangement of neighbouring LPEs affects the potential energy. We find that the SIG phase, with the least random LPE arrangement, has the lowest potential energy, thereby making it the thermodynamically stable structure among these three, followed by the HAC and HQC phases.

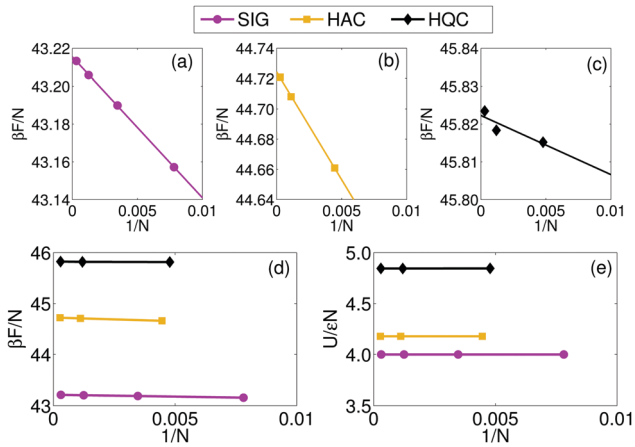

Fig. 9 Variation of Helmholtz free energy per particle $\beta F/N$ as a function of system size for (a) sigma (SIG) (b) approximant (HAC) (c) quasicrystal (HQC) phases and (d) combined view of all three phases (e) variation of potential energy per particle $\beta U/N$ as a function of system size. The values were calculated for the phases with a density $\rho^* = N\sigma^2/A = 1.03$ at temperature $T^* = 0.11$ for the HCSS system with shoulder width $\delta = 1.95\sigma_{HD}$. The lines in (a–c) are linear fit to the data points.

Even though we have seen than the SIG phase has a lower free energy than the HQC and QCS phases, it is important to point out here that the presence of phasonic movements in these tilings contribute to the configurational entropy of these quasicrystals.[69,73,74] In the case of the HQC, the configurational entropy that accounts for the distinct number of configurations has a maximum value of $S_{config}/k_BA = 0.12934$,[75] which is much smaller than the difference between the free energies of the SIG and HQC phases. Considering this value, we do not expect the configurational entropy of the square-triangle-shield tiling to exceed the difference between the free energies of the SIG and QCS phase, *i.e.*, $S_{config}/k_BA > 0.5$. We thus conclude that the SIG phase is thermodynamically more stable than all the other phases with dodecagonal symmetry considered in this study, namely HAC, HQC and QCS phases.

C. Formation of the stripe phase

The most striking feature of the phase diagram presented in Fig. 3 is the phase behaviour observed at low density and temperatures, especially the formation of the stripe (STR) phase. Such spontaneous pattern formations are observed in core–corona systems when the size of the corona is similar or much larger than that of the core.[32–36]

Stripe formation in purely repulsive systems is driven by the minimization of the system's potential energy. The configuration of the STR phase as given in Fig. 3 shows that each particle has overlapping coronas with two other neighbouring particles along the stripe. However, the stripes are spaced such that the distance between them is larger than the size of the corona and thus, there is no overlap between the coronas between adjacent stripes. In other words, the effective repulsive length scales are the diameter of the hard core σ_{HD} along the stripes and the soft-shoulder diameter δ orthogonal to the stripes. As a consequence, each particle essentially has only two neighbours. This is energetically more favourable than a structure with equally spaced particles in which the shoulder of each particle partially or completely overlaps with all of its neighbours.

In order to study the formation of the STR phase in the system, we first obtain the EOS of the different phases by compressing the system starting from an isotropic fluid phase and by expanding the system starting with the HC and MDH phases. In Fig. 10, we plot the EOS obtained at temperatures $T^* = 0.18$, 0.15 and 0.12. First, we recognise the formation of two hexagonal phases: (1) the LDH phase sandwiched in between two FL phases by two first-order phase transitions at temperature $T^* = 0.12$ and (2) the MDH at higher densities, for which at all three temperatures the EOSs lie on top of each other (and thus are not individually identifiable in the figure). The EOS of the HC phase at $T^* = 0.12$ and 0.15 lie on top of each other, whereas the HC is not stable at $T^* = 0.18$. We also notice first-order phase transitions between the HC and the STR at $T^* = 0.12$, 0.15 and

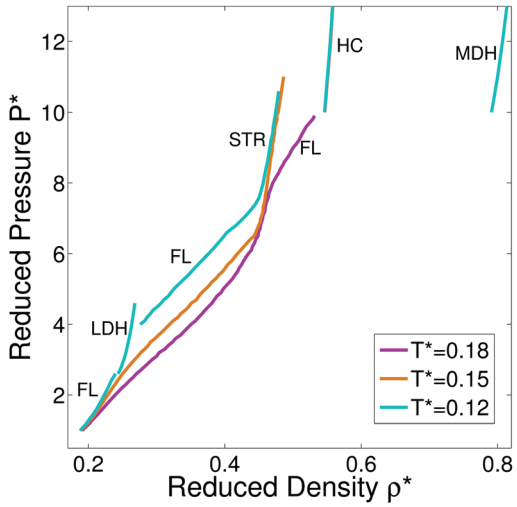

Fig. 10 Equation of state (pressure $P^* = \beta P \sigma_{HD}^2$ as a function of density $\rho^* = N\sigma_{HD}^2/A$) of a HCSS system with shoulder width $\delta = 1.95\sigma_{HD}$ at temperatures $T^* = k_BT/\varepsilon = 0.18$, 0.15, and 0.12. The phases observed are fluid (FL), low-density hexagonal (LDH), stripe (STR), honeycomb (HC) and medium-density hexagonal (MDH) phases. The equations of state of the MDH phase at all three temperatures lie on top of each other. The equations of state of the HC phase at $T^* = 0.12$ and 0.15 also lie on top of each other, while this phase is absent at $T^* = 0.18$.

between MDH and FL at $T^* = 0.18$. The confounding feature of the EOS at all these temperatures is the continuous transition from the FL phase to the STR phase. This also applies to the further re-entrant transition from the STR phase to the FL phase with increasing density at the highest temperature $T^* = 0.18$. The only observed development in the EOS is the change in slope during these transitions. However, this cannot be used to determine the transition from the FL to the STR phase and we therefore resort to order parameters. The parameters used for this include the number of clusters in the system, the number of neighbours of the particles in the system and the anisotropic scaling index method as described in Section II C. The method of calculation and behaviour of these three parameters during this phase transition are explained below.

The first parameter we use is the normalised cluster size N_c/N as a function of pressure P^*, where N_c is the average cluster size in number of particles and N is the total number of particles in the system. In other words, the normalised cluster size N_c/N is the inverse of the number of clusters in the system and varies from approximately zero in the case of the FL phase to unity in the case of the STR phase. The second parameter consists of studying the probability distribution of the average number of neighbours per particle $P(N_n)$ at different pressures P^*. The basis of using this as an order parameter emerges from the fact that the particles in the STR phase have on average two neighbours, which is not a requisite in the FL phase. Finally, the scalar order parameter $\Delta\alpha$ is the difference between the distributions of $P_\perp(\alpha)$ and $P_\parallel(\alpha)$. The distributions coincide with each other for an isotropic structure like the fluid phase, but not for an anisotropic structure like the stripe phase. Thus, $\Delta\alpha$ is non-zero for anisotropic structures and it vanishes for isotropic structures. We believe that as each of these three parameters address a different property of the system and especially of the STR phase; we obtain complementary insights about the STR phase by investigating all of them.

Let us begin with addressing the formation of the STR phase from the FL phase. As shown in the EOS in Fig. 10, this fluid-to-stripe (FL–STR) phase transition was observed at all three temperatures studied. Here, we will explore this transition at $T^* = 0.15$. The various aspects of monitoring this phase transition is shown in Fig. 11. Let us first take a qualitative look at this

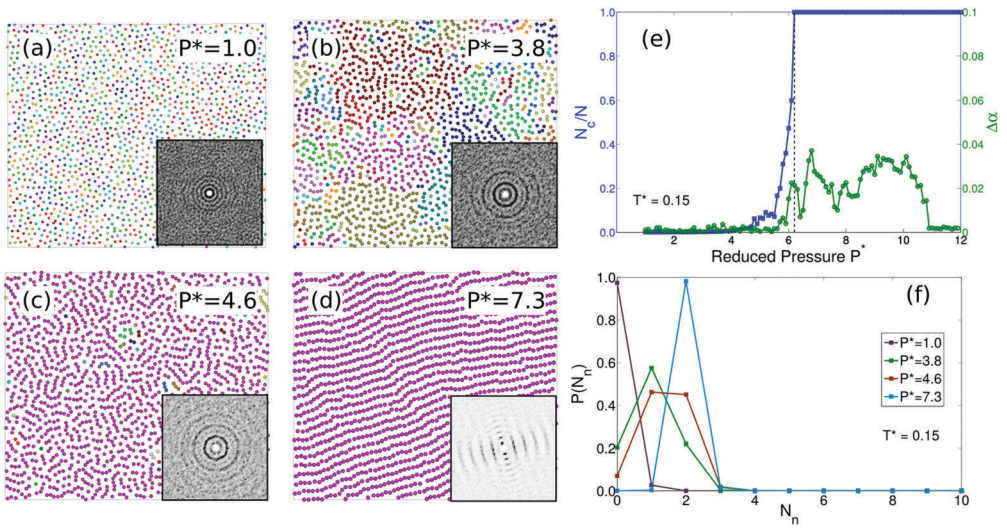

Fig. 11 Monitoring the fluid-to-stripe (FL–STR) phase transition in a HCSS system with shoulder width $\delta = 1.95\sigma_{HD}$ at temperature $T^* = k_BT/\varepsilon = 0.15$. (a–d) Typical configurations as obtained from Monte Carlo simulations at different pressures $P^* = \beta P \sigma_{HD}^2$ as labelled. Colours represent different clusters. The insets show the corresponding diffraction patterns. (e) The normalised cluster size N_c/N and the scalar order parameter $\Delta\alpha$ as a function of the reduced pressure P^*. N_c is the average cluster size and N is the total number of particles in the system. (f) Probability distribution of the number of nearest neighbours per particle $P(N_n)$ at varying pressures P^* as labelled.

transition by observing the typical configurations obtained using Monte Carlo simulations at different pressures. This is shown in Fig. 11a–d. Each cluster is represented in a different colour. As shown in Fig. 11b and c, a cluster can also consist of multiple strings. From Fig. 11a–d, we see that the number of clusters decreases with increasing pressure and that the stripes essentially form a percolating cluster. We can differentiate between the FL and the STR phase using the calculated diffraction pattern shown as insets; the ones corresponding to the FL phase show the presence of isotropic rings, while that of the STR phase shows spots which are arranged in layers. We, therefore, can use the number of clusters in the system as a parameter to determine the FL to STR transition. In Fig. 11e, we present the resulting cluster size distribution as a function of pressure P^*. We notice that the distribution exhibits a rapid change to unity at $P^* \sim 6.2$ indicating the formation of a single cluster in the system. However, the formation of a percolating cluster does not entirely refer to the formation of a STR phase. Thus, in this same plot, we also show the variation of the scalar order parameter $\Delta\alpha$ as a function of pressure P^*. As previously discussed, a non-zero value of $\Delta\alpha$ relates to an anisotropic layered structure. We indeed do notice that $\Delta\alpha$ becomes non-zero close to the transition pressure of the cluster size distribution confirming the phase formed to be STR and then vanishes at $P^* \sim 10.9$ with the formation of the MDH phase. Furthermore, we verify the string nature of these layers by studying the probability distribution of the average number of neighbours per particle $P(N_n)$ as a function of the number of neighbours N_n at different pressures P^*. This is shown in Fig. 11f where the pressures correspond to the ones in Fig. 11a–d. As expected, the average number of neighbours per particle increases with increasing pressure. The average number of neighbours per particle N_n goes from zero in the FL phase at $P^* = 1.0$ to unity at $P^* = 3.8$ and to a value of two at $P^* = 7.3$, where the STR phase is observed. This verifies the energetic driving force of the formation of the STR by having only two nearest neighbours per particle.

Now, let us study the inverse transition, *i.e.* formation of the FL phase from the STR phase at higher densities. As shown in the EOS in Fig. 10, of the three temperatures studied, we observe this stripe-to-fluid (STR–FL) phase transition only at $T^* = 0.18$. Similar to the previous case, we show the various aspects of this phase transition in Fig. 12. In Fig. 12a, we show the behaviour of N_c/N and $\Delta\alpha$ as a function of pressure P^*. As expected, we notice the discontinuous change of N_c/N to unity with the formation of a single cluster and the non-zero value of $\Delta\alpha$ signalling a stripe phase at pressures $5.9 < P^* < 8.3$. Then, we analyse the probability distributions of neighbours $P(N_n)$ at different pressures P^* given in Fig. 12b. For convenience and comparison, typical configurations corresponding to these pressures are given in Fig. 12c–f. Here, the particles are coloured according to the number of neighbours in contrast to Fig. 11, where the colours denote distinct clusters. The colour legend is at the bottom of the figure. From the $P(N_n)$ distributions and the particle configurations, we observe that the STR phase with $N_n = 2$ is obtained at reduced pressure $P^* = 7.0$ and at the highest pressure of $P^* = 10.1$, the system forms a hexagonal structure with $N_n = 6$. As evident from the diffraction pattern given in the insets of Fig. 12d and e, a FL phase is formed at pressures intermediate to these. From the $P(N_n)$ distribution given in Fig. 12b, we note that the FL phase has an average of three neighbours per particle and starts to form at $P^* = 8.6$. The 'coexisting' nature of this structure with FL and STR is evident from Fig. 12d, where short stripe segments in green are connected by yellow and blue particles. This implies that the stripes

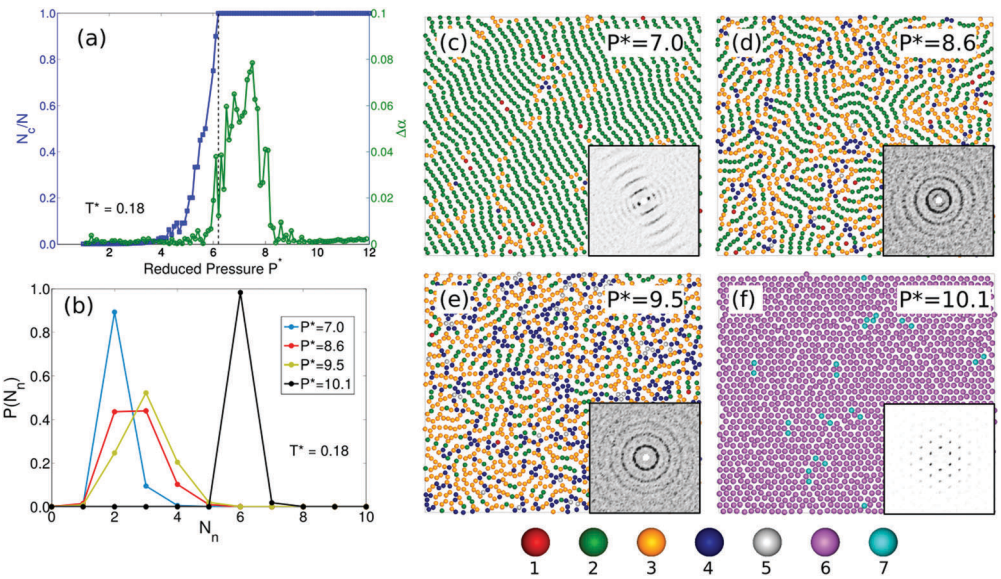

Fig. 12 Monitoring the stripe-to-fluid (STR–FL) phase transition in a HCSS system with shoulder width $\delta = 1.95\sigma_{HD}$ at temperature $T^* = k_BT/\varepsilon = 0.18$. (a) The normalised cluster size N_c/N and the scalar order parameter $\Delta\alpha$ as a function of the reduced pressure $P^* = \beta P\sigma_{HD}^2$. N_c is the average cluster size and N is the total number of particles in the system. (b) Probability distribution of the number of nearest neighbours per particle $P(N_n)$ at varying pressures P^* as labelled. (c–f) Typical configurations as obtained from Monte Carlo simulations corresponding to the pressures P^* in (b). The particles are coloured according to the number of neighbours as shown in the legend at the bottom of the panel. The insets show the corresponding diffraction patterns.

become shorter as the system becomes more fluid-like with increasing pressure.

The above observations of discontinuity in the N_c/N and $\Delta\alpha$ distributions and the co-existing nature of the $P(N_n)$ at certain pressures hint at a first-order transition between the FL and STR phases. However, to ascertain this speculation further, we assess the FL–STR transition by using the specific heat at constant volume C_v as described in Section II B and the fraction of defects. Defects in the structure are defined as particles which have other than two neighbouring particles. We study the system at constant density $\rho^* = 0.46$, where we find that the system undergoes a sharp transition from a STR phase to a FL phase upon increasing the temperature. The C_v as a function of temperature T^* is plotted in Fig. 13a. In Fig. 13b, we plot the variation of the fraction of defects along the same transition. The C_v shows a λ-shaped cusp around the transition temperature $T_{STR-FL}^* = 0.187$, from which one may conclude that the transition is likely first-order in nature. However, even though we find a substantial difference between the fractions of defects in the STR and FL phases, the change from STR to FL is not as abrupt as in case of C_v. This change in the fraction of defects extends over a range of temperatures between $T_{STR-FL}^* \pm 0.01$. This difference between the two phases in terms of the defects is shown in Fig. 13c and d. Here, we show the configurations obtained at temperatures $T^* = 0.18$ and 0.19, where the particles are coloured according to the number of neighbours as given in the legend at the bottom of the figure. At temperatures lower than T_{STR-FL}^*, a single percolating network of parallel stripes mostly containing two neighbouring particles is observed and at temperature $T^* > T_{STR-FL}^*$, the particles form winding structures consisting of small segments of stripes. This continuous melting of the STR phase to an isotropic FL fluid phase mediated by defects (dislocations or disclinations) bears resemblances to the scenario studied in detail by Toner and Nelson,[76,77] also known as the Kosterlitz–Thouless (K–T) transition. In general, the K–T transition can be described to occur between a phase with order in the orientation of the bond angles and a phase which is devoid of such an order.

Thus, we evaluate if the STR phase possess a two-fold bond orientational symmetry and subsequently analyse the STR to FL phase transition by calculating the positional correlation function $g(r)$ and bond orientational correlation $g_2(r)$ function. These correlation functions as a function of temperature are given in Fig. 14a and b. Firstly, we observe that the positional correlation function shown in Fig. 14a decays exponentially through the entire range of temperatures. This indicates that both the STR and the FL phases do not possess long-range positional order. Further, the bond orientational correlation function plotted in Fig. 14b reaches a constant value at lower temperatures indicating that the STR phase formed at these temperatures possess quasi long-range bond orientational order, *i.e.* two-fold rotational symmetry. With increasing temperature, the bond orientational correlation function starts to decay rapidly. This represents the loss of the bond orientational order in the system. Consequently, the transition from the STR to the FL phase can be described as a elimination of the bond orientational order of the system, *i.e.* a K–T

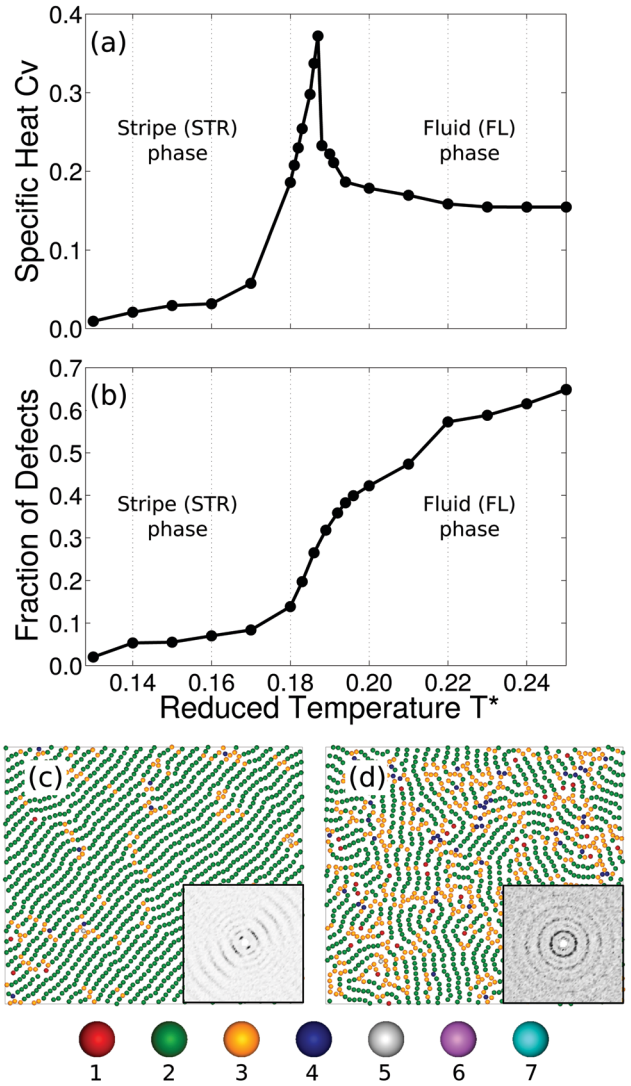

Fig. 13 Phase transition from the stripe (STR) phase to the fluid (FL) phase for a HCSS system with a shoulder width $\delta = 1.95\sigma_{HD}$ and density $\rho^* = N\sigma_{HD}^2/A = 0.46$: (a) specific heat C_v at constant volume and (b) fraction of defects as a function of reduced temperature T^*. Typical configurations obtained at temperature $T^* = k_BT/\varepsilon$ (c) 0.18 (d) 0.19, where the particles are coloured according to the number of neighbours as shown in the legend at the bottom of the figure.

transition. Additionally, we also verify if the same holds for the FL to STR transition described in Fig. 11. For this, we plot the positional and bond orientational functions at varying densities for a constant temperature $T^* = 0.15$. This is given in Fig. 14c and d. We, again, observe the presence of quasi-long range bond orientational order correlations in the STR phase and the absence of long-range positional order in both the STR and FL phases, thereby providing support for a K–T phase transition. Also, the density at which the transition from the FL to the STR phase takes place, *i.e.* $\rho^* \sim 0.43$, agrees well with the phase diagram given in Fig. 3.

In conclusion, we find that the STR phase displays quasi-long range bond orientational order and short-range positional order which melts to an isotropic FL phase with no bond-orientational and positional order upon increasing the temperature

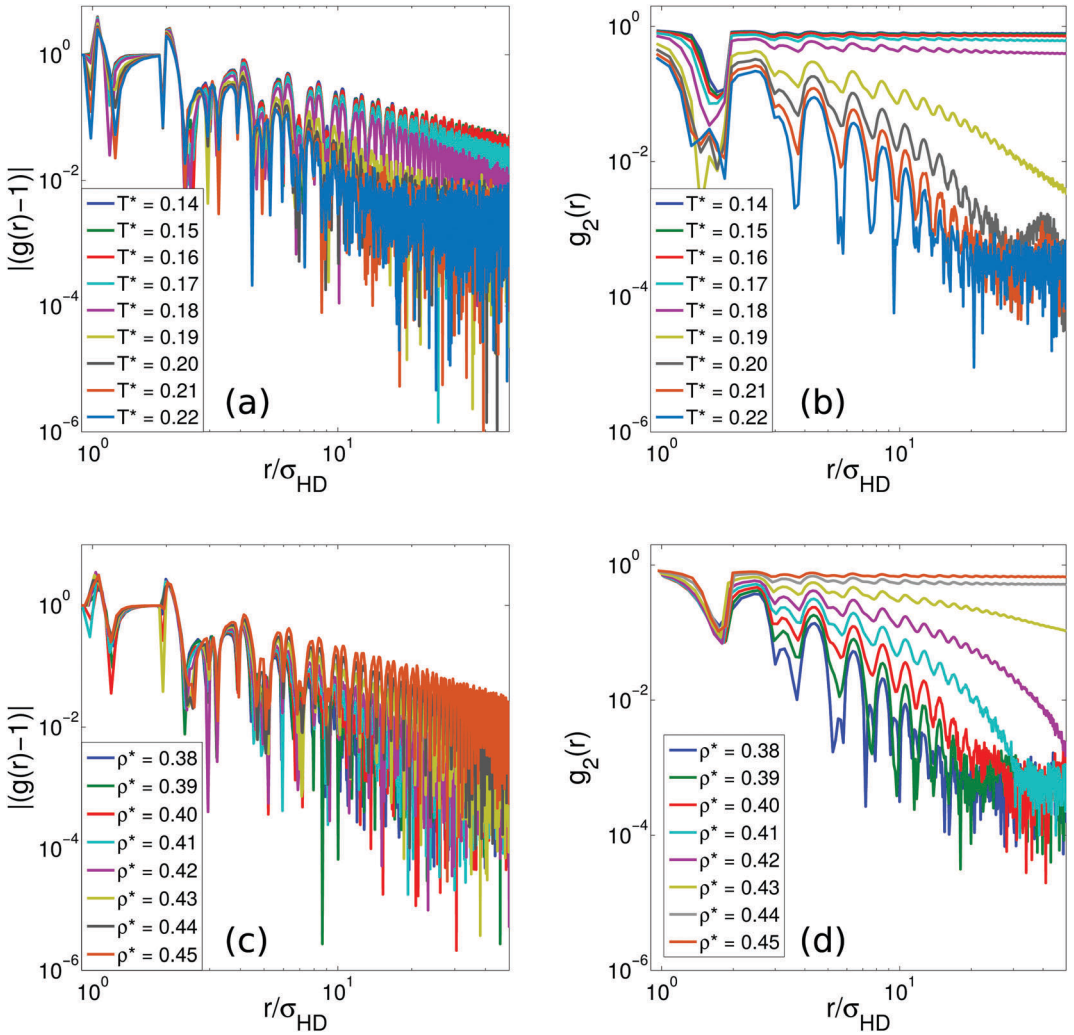

Fig. 14 (a and c) Positional correlation function $g(r)$ and (b and d) bond orientational correlation function $g_2(r)$ describing the phase transition from the stripe (STR) phase to an isotropic fluid (FL) phase for a HCSS system with a shoulder width $\delta = 1.95\sigma_{HD}$ calculated at: (a and b) different temperatures at constant density $\rho^* = N\sigma_{HD}{}^2/A = 0.46$ and (b) different densities at temperature $T^* = k_BT/\varepsilon = 0.15$. All plots are in log–log scale.

or decreasing the density. Although we observe a sharp cusp in the specific heat C_v, the continuous change in the defect concentration as well as the loss of bond orientational order provide evidence for a K–T transition.

D. Stability of the honeycomb phase

Another interesting feature of this system is the formation of a honeycomb (HC) phase wedged between the stripe (STR) and medium-density hexagonal (MDH) phases. HC phases have previously been reported to form in patchy colloids,[17] DNA nanostructures[78,79] and binary mixtures of particles under external electric[3,4] and magnetic fields.[8] Thus, it is fascinating that our mono-disperse core–corona system with no external forces forms a stable honeycomb lattice. In this core–corona system, formation of the HC phase from the STR phase with increasing density is a logical step forward. This can be seen as an increase in the number of neighbours per particle from two in the STR to three in the HC phase. In order to evaluate the thermodynamic stability of the HC phase, we plot the chemical potential $\beta\mu$ of the STR, HC and MDH phases, as obtained from the free-energy calculations, as a function of pressure $P^* = \beta P\sigma_{HD}{}^2$. In Fig. 15, we show this plot at $T^* = 0.15$. As expected, we find that the HC phase is more stable than the STR–MDH two-phase coexistence.

The enigma in the stability of the HC phase is introduced by the previous report of formation of a low-density dodecagonal quasicrystal (LQC) by Dotera *et al.*[40] This quasicrystal was reported to form when cooling a hexagonal phase with density $\rho^* = 0.55$ to a lower temperature $T^* \leq 0.154$.[40] However, these conditions of density and temperature correspond to the stability region of the HC phase calculated above. In order to determine which of these two phases, LQC and HC, is indeed stable, we perform direct coexistence simulations. We started the simulations by juxtaposing LQC structure with $\rho^* = 0.55$ and MDH structure with $\rho^* = 0.79$ in a simulation box which results in a overall density of $\rho^* = 0.65$. This initial configuration is shown in Fig. 16a. The particles here are coloured according to the number of neighbours given in the legend at the bottom. The diffraction pattern given in the inset confirms the dodecagonal symmetry of

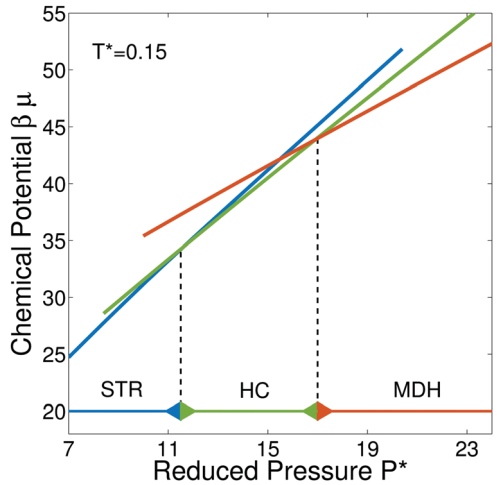

Fig. 15 The chemical potential $\beta\mu$ as a function of reduced pressure $P^* = \beta P\sigma_{HD}^2$ at temperature $T^* = k_BT/\varepsilon = 0.15$ for the HCSS system with $\delta = 1.95\sigma_{HD}$. The stable phases are stripe (STR), honeycomb (HC) and medium-density hexagonal (HDH) phases. The arrows at the bottom denote the phase stability regions.

the LQC. The final configuration obtained from the simulation is given in Fig. 16b. We observe that the LQC has transformed to the HC phase as corroborated by the particle neighbours and the corresponding diffraction pattern. This confirms that the HC phase is thermodynamically stable and that the LQC is, in fact, kinetically formed in the two-phase coexistence region between the HC and MDH phases.

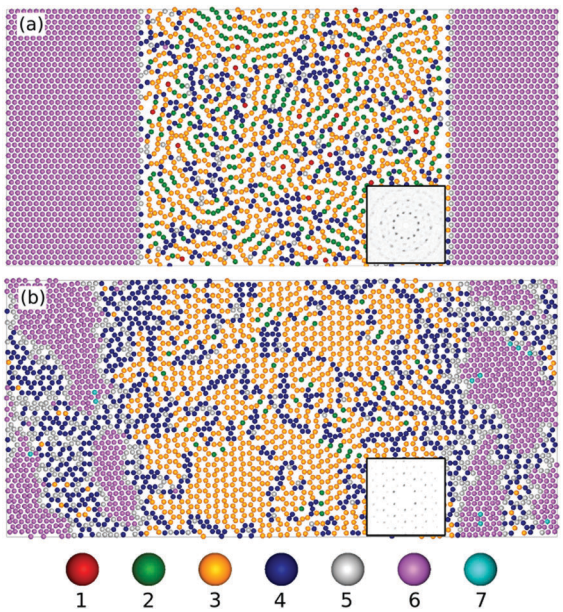

Fig. 16 Direct coexistence simulations carried out to evaluate the relative stability between the low-density quasicrystal (LQC), honeycomb (HC) and medium-density hexagonal (MDH) phases at a temperature $T^* = k_BT/\varepsilon = 0.15$ and density $\rho^* = N\sigma_{HD}^2/A = 0.65$ (a) initial configuration consisting of MDH and LQC (b) final configuration consisting of MDH and HC phases. The particles are coloured according to the number of neighbours as shown in the legend at the bottom of the figure. The insets show the diffraction patterns calculated for the non-MDH region of the simulation box.

IV. Conclusions

To summarise, we study the phase behaviour of a system consisting of particles with a core–corona molecular architecture using Monte Carlo simulations and free-energy calculations. The model is described by an inter-particle pair potential consisting of a hard core of diameter σ_{HD} and a purely repulsive soft shoulder of diameter $\delta = 1.95\sigma_{HD}$. We observe a rich phase behaviour consisting of a fluid phase, a striped mesophase, honeycomb, sigma and three distinct hexagonal phases. We find the different phases are energetically stabilised.

At higher densities, we find that the sigma phase is energetically stabilised with respect to the random-tiling dodecagonal quasicrystals with square-triangle and square-triangle-shield tilings and the square-triangle approximant. This is in contrast to the entropic stabilisation of the random-tiling dodecagonal quasicrystal consisting of squares and triangles previously reported at $\delta = 1.4\sigma_{HD}$.[38] Due to the larger shoulder width, the position of particles beyond the second nearest neighbours play an important role in the potential energy of the concerned structure. Thus, in contrast to the system at $\delta = 1.4\sigma_{HD}$, there exists a difference in potential energies between the sigma phase, the quasicrystal and the approximant resulting from a variation in the arrangement of their local particle environments.

At lower densities, the formation of these phases is driven by minimising the number of neighbours per particle. This results in the formation of stripe and honeycomb phases which respectively have two and three neighbours. It is interesting to point out that the next logical structure with four neighbours, *i.e.* square, is not formed in our system.[4,17] Instead we find the formation of a six particle-coordinated medium-density hexagonal phase. This is because the square shoulder of the central particle of a square encompasses also the diagonal particles, which results in eight neighbours per particle. Thus, this does not provide any energetic incentive over the hexagonal structure. Additionally, our results provide support that the melting of the stripe phase into an isotropic fluid phase is mediated by defects and resembles a Kosterlitz–Thouless (K–T) phase transition. Further, we deduce that the low-density dodecagonal quasicrystal structure that was previously reported for this system[40] is in fact metastable. It is formed in the two-phase coexistence region of the honeycomb and medium-density hexagonal phase.

In addition to the interesting phase behaviour of these phases, the honeycomb[29] and sigma[31] phases are interesting for their applications as photonic crystals. We hope that our results confirming the formation of stripe, honeycomb and sigma phases at different densities in a single system will stimulate experimental investigations on the phase behaviour and self-assembly of such systems containing particles with a core–corona architecture.

Acknowledgements

This work is part of the Industrial Partnership Programme "Computational Sciences for Energy Research" (12CSER004) of the Foundation for Fundamental Research on Matter (FOM), which is part of the Netherlands Organisation for Scientific

Research (NWO). This research programme is co-financed by Shell Global Solutions International B.V. We thank Vasileios Pyrimidis and Guido Avvisati for critical reading of the manuscript.

References

1 M. Seul and R. Wolfe, *Phys. Rev. A: At., Mol., Opt. Phys.*, 1992, **46**, 7519.
2 A. Yethiraj and A. van Blaaderen, *Nature*, 2003, **421**, 513.
3 W. D. Ristenpart, I. A. Aksay and D. A. Saville, *Phys. Rev. Lett.*, 2003, **90**, 128303.
4 I. Varga, F. Kun and K. F. Pál, *Phys. Rev. E: Stat., Nonlinear, Soft Matter Phys.*, 2004, **69**, 2.
5 I. Varga and F. Kun, *Philos. Mag.*, 2005, **86**, 2011.
6 A. P. Hynninen and M. Dijkstra, *Phys. Rev. Lett.*, 2005, **94**, 138303.
7 N. Osterman, D. Babic, I. Poberaj, J. Dobnikar and P. Ziherl, *Phys. Rev. Lett.*, 2009, **99**, 248301.
8 K. S. Khalil, A. Sagastegui, Y. Li, M. A. Tahir, J. E. S. Socolar, B. J. Wiley and B. B. Yellen, *Nat. Commun.*, 2012, **3**, 794.
9 P. Liu, J. W. J. de Folter, A. V. Petukhov and A. P. Philipse, *Soft Matter*, 2015, **11**, 6201.
10 F. Liu, B. Chen, U. Baumeister, X. Zeng, G. Ungar and C. Tschierske, *J. Am. Chem. Soc.*, 2007, **129**, 9578.
11 A. Haji-Akbari, M. Engel and S. C. Glotzer, *Phys. Rev. Lett.*, 2011, **107**, 215702.
12 A. Haji-Akbari, M. Engel and S. C. Glotzer, *J. Chem. Phys.*, 2011, **135**, 1.
13 X. Ye, J. Chen, M. E. Irrgang, M. Engel, A. Dong, S. C. Glotzer and C. B. Murray, *Nat. Mater.*, 2017, **16**, 214.
14 D. V. Talapin, E. V. Shevchenko, M. I. Bodnarchuk, X. Ye, J. Chen and C. B. Murray, *Nature*, 2009, **461**, 964.
15 M. I. Bodnarchuk, R. Erni, F. Krumeich and M. V. Kovalenko, *Nano Lett.*, 2013, **13**, 1699.
16 Q. Chen, S. C. Bae and S. Granick, *Nature*, 2011, **469**, 381.
17 C. S. Dias, N. A. M. Araújo and M. M. T. Gama, *Mol. Phys.*, 2015, **113**, 1069.
18 S. Keller and H. McConnell, *Phys. Rev. Lett.*, 1999, **82**, 1602.
19 J. Maclennan and M. Seul, *Phys. Rev. Lett.*, 1992, **69**, 2082.
20 C. L. Phillips and G. A. Voth, *Soft Matter*, 2013, **9**, 8552.
21 X. Zeng, G. Ungar, Y. Liu, V. Percec, A. E. Dulcey and J. K. Hobbs, *Nature*, 2004, **428**, 157.
22 A. Takano, W. Kawashima, A. Noro, Y. Isono, N. Tanaka, T. Dotera and Y. Matsushita, *J. Polym. Sci., Part B: Polym. Phys.*, 2005, **43**, 2427.
23 T. Dotera and T. Gemma, *Philos. Mag.*, 2006, **86**, 1085.
24 K. Hayashida, T. Dotera, A. Takano and Y. Matsushita, *Phys. Rev. Lett.*, 2007, **98**, 195502.
25 S. Lee, M. J. Bluemle and F. S. Bates, *Science*, 2010, **330**, 349.
26 S. Fischer and A. Exner, *Proc. Natl. Acad. Sci. U. S. A.*, 2011, **108**, 1810.
27 M. J. Liu, W. H. Li, F. Qiu and A.-C. Shi, *Soft Matter*, 2016, **12**, 6412.
28 M. Zoorob, M. Charlton, G. Parker, J. Baumberg and M. Netti, *Nature*, 2000, **404**, 740.
29 T.-I. Weng and G. Y. Guo, *J. Appl. Phys.*, 2006, **99**, 093102.
30 A. J. Garcia-Adeva, *New J. Phys.*, 2006, **8**, 86.
31 K. Ueda, T. Dotera and T. Gemma, *Phys. Rev. B: Condens. Matter Mater. Phys.*, 2007, **75**, 195122.
32 G. Malescio and G. Pellicane, *Nat. Mater.*, 2003, **2**, 97.
33 P. Camp, *Phys. Rev. E: Stat., Nonlinear, Soft Matter Phys.*, 2003, **68**, 061506.
34 G. Malescio and G. Pellicane, *Phys. Rev. E: Stat., Nonlinear, Soft Matter Phys.*, 2004, **70**, 021202.
35 J. Fornleitner and G. Kahl, *J. Phys.: Condens. Matter*, 2010, **22**, 104118.
36 M. Singh, H. Liu, S. K. Kumar, A. Ganguly and C. Chakravarty, *J. Chem. Phys.*, 2010, **132**, 074503.
37 T. Dotera, *Isr. J. Chem.*, 2011, **51**, 1197.
38 H. Pattabhiraman, A. P. Gantapara and M. Dijkstra, *J. Chem. Phys.*, 2015, 164905.
39 E. A. Jagla, *Phys. Rev. E: Stat. Phys., Plasmas, Fluids, Relat. Interdiscip. Top.*, 1998, **58**, 11.
40 T. Dotera, T. Oshiro and P. Ziherl, *Nature*, 2014, **506**, 208.
41 H. G. Schoberth, H. Emmerich, M. Holzinger, M. Dulle, S. Förster and T. Gruhn, *Soft Matter*, 2016, **12**, 7644.
42 A. Skibinsky, S. V. Buldyrev, A. Scala, S. Havlin and H. E. Stanley, *Phys. Rev. E: Stat. Phys., Plasmas, Fluids, Relat. Interdiscip. Top.*, 1999, **60**, 2664.
43 L. Q. Costa Campos, C. C. de Souza Silva and S. W. S. Apolinario, *Phys. Rev. E: Stat., Nonlinear, Soft Matter Phys.*, 2012, **86**, 051402.
44 C. I. Mendoza and E. Batta, *EPL*, 2009, **85**, 56004.
45 G. Das, N. Gnan, F. Sciortino and E. Zaccarelli, *J. Chem. Phys.*, 2013, **138**, 134501.
46 M. Engel and H.-R. Trebin, *Phys. Rev. Lett.*, 2007, **98**, 225505.
47 M. Engel, P. F. Damasceno, C. L. Phillips and S. C. Glotzer, *Nat. Mater.*, 2014, **14**, 109.
48 R. Lifshitz and D. Petrich, *Phys. Rev. Lett.*, 1997, **79**, 1261.
49 A. M. Rucklidge and M. Silber, *Phys. Rev. E: Stat., Nonlinear, Soft Matter Phys.*, 2007, **75**, 1.
50 K. Barkan, H. Diamant and R. Lifshitz, *Phys. Rev. B: Condens. Matter Mater. Phys.*, 2011, **83**, 172201.
51 A. J. Archer, A. M. Rucklidge and E. Knobloch, *Phys. Rev. Lett.*, 2013, **111**, 165501.
52 A. J. Archer, A. M. Rucklidge and E. Knobloch, *Phys. Rev. E: Stat., Nonlinear, Soft Matter Phys.*, 2015, **92**, 012324.
53 Y. Norizoe and T. Kawakatsu, *Europhys. Lett.*, 2005, **72**, 583.
54 Y. Norizoe and T. Kawakatsu, *J. Chem. Phys.*, 2012, **137**, 024904.
55 K. Barkan, M. Engel and R. Lifshitz, *Phys. Rev. Lett.*, 2014, **113**, 1.
56 D. Frenkel and B. Smit, *Understanding molecular simulation: From Algorithm to Applications*, Academic Press, 1996, ISBN 0-12-267351-4.
57 C. Vega and E. Sanz, *J. Phys.: Condens. Matter*, 2008, 153101.
58 A. M. Almudallal, S. V. Buldyrev and I. Saika-Voivod, *J. Chem. Phys.*, 2012, **137**, 034507.
59 J. M. Polson, E. Trizac, S. Pronk and D. Frenkel, *J. Chem. Phys.*, 2000, **112**, 5339.
60 T. Schilling and F. Schmid, *J. Chem. Phys.*, 2009, **131**, 231102.
61 F. Schmid and T. Schilling, *Phys. Procedia*, 2010, **4**, 131.
62 H. Weber, D. Marx and K. Binder, *Phys. Rev. B: Condens. Matter Mater. Phys.*, 1995, **51**, 14636.

63 M. N. van der Linden, J. Doye and A. Louis, *J. Chem. Phys.*, 2012, **136**, 54904.
64 C. Räth, W. Bunk, M. B. Huber, G. E. Morfill, J. Retzlaff and P. Schuecker, *Mon. Not. R. Astron. Soc.*, 2002, **337**, 413.
65 A. V. Ivlev, G. E. Morfill, H. M. Thomas, C. Räth, G. Joyce, P. Huber, R. Kompaneets, V. E. Fortov, A. M. Lipaev and V. I. Molotkov, *et al.*, *Phys. Rev. Lett.*, 2008, **100**, 1.
66 J. A. Millan and S. C. Glotzer, *Soft Matter*, 2015, **11**, 1386.
67 M. Oxborrow and C. Henley, *Phys. Rev. B: Condens. Matter Mater. Phys.*, 1993, **48**, 6966.
68 M. O'Keeffe and M. M. J. Treacy, *Acta Crystallogr., Sect. A: Found. Crystallogr.*, 2010, **66**, 5.
69 J. Roth and F. Gähler, *Eur. Phys. J. B*, 1998, **6**, 425.
70 M. Engel, PhD thesis, Universitat Stuttgart, 2008.
71 C. R. Iacovella, A. S. Keys and S. C. Glotzer, *Proc. Natl. Acad. Sci. U. S. A.*, 2011, **108**, 9.
72 S. B. Rochal, O. V. Konevtsova, I. A. Shevchenko and V. Lorman, *Soft Matter*, 2015, **12**, 1238.
73 M. Engel, *Phys. Rev. Lett.*, 2011, **106**, 3.
74 T. Dotera, *J. Polym. Sci., Part B: Polym. Phys.*, 2012, **50**, 155.
75 M. Widom, *Phys. Rev. Lett.*, 1993, **70**, 2094.
76 J. Toner and D. R. Nelson, *Phys. Rev. B: Condens. Matter Mater. Phys.*, 1981, **23**, 316.
77 D. R. Nelson and J. Toner, *Phys. Rev. B: Condens. Matter Mater. Phys.*, 1981, **24**, 363.
78 Y. He, Y. Chen, H. Liu, A. E. Ribbe and C. Mao, *J. Am. Chem. Soc.*, 2005, **127**, 12202.
79 Y. He and C. Mao, *Chem. Commun.*, 2006, 968–969.

